数理解析研究所講究録
第2009巻 2016年 27-43

A computational study on the generation of the Coanda effect in a mock heart chamber

A. Quaini[a*], R. Glowinski[a,b] and S. Čanić[a]

[a] *Department of Mathematics, University of Houston, Houston, TX 77204, USA*
[b] *Department of Mathematics, Hong-Kong Baptist University, Hong-Kong*

Abstract

We present a numerical study of laminar incompressible flows in two-dimensional and three-dimensional contraction-expansion channels. The aim is to understand the causes of the so-called Coanda effect (i.e., the tendency of a fluid jet to be attracted to a surface) in order to reproduce wall-hugging jets in a mock heart chamber constructed to improve the diagnosis of mitral valve regurgitation. First, we validate the critical Reynolds number for the onset of the Coanda effect (also known as symmetry-breaking bifurcation) given by our computations against the values found in the literature. Excellent agreement is found. Then, we considered flow in a section of the mock heart chamber and showed how a pronounced Coanda effect is possible only with some modifications of the contraction channel geometry. Finally, we propose a 3D mock heart chamber in which quasi-2D flow is possible, thereby allowing the Coanda effect at the low Reynolds numbers for which it is observed in 2D.

1 Introduction

Coanda effect is a phenomenon that is described in the scientific literature as the tendency of a fluid jet to be attracted to a nearby surface [27, 29], see Figure 1. The principle was named after Romanian aerodynamics pioneer Henri Coanda, who was the first to recognize the practical application of the phenomenon in aircraft development.

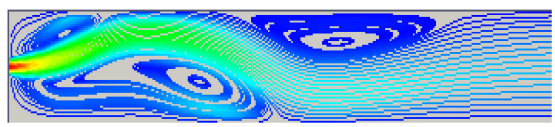

Figure 1: Steady state solution for flow in a sudden expansion with a $1:6$ expansion at $Re = 133.3$. The jet hugs the upper wall of the expansion chamber.

Most recently, Coanda effect became popular in cardiology where it has been used to explain the wall hugging jets in certain cases of mitral valve regurgitation. Mitral regurgitation (MR) is a valvular disease characterized by abnormal leaking of blood through the mitral valve from the left ventricle into the left atrium of the heart. MR can lead to atrial arrhythmias, pulmonary artery hypertension, congestive heart failure, and death. Diagnosis of mitral regurgitation is often performed using color Doppler echocardiography. Figure 2(a) shows the echocardiographic image of a jet flowing in the center of the left atrium (central jet), while Figure 2(b) shows the echocardiographic image of a jet hugging the wall of the left atrium (eccentric jet), known as the Coanda effect.

*Corresponding author. Email: quaini@math.uh.edu

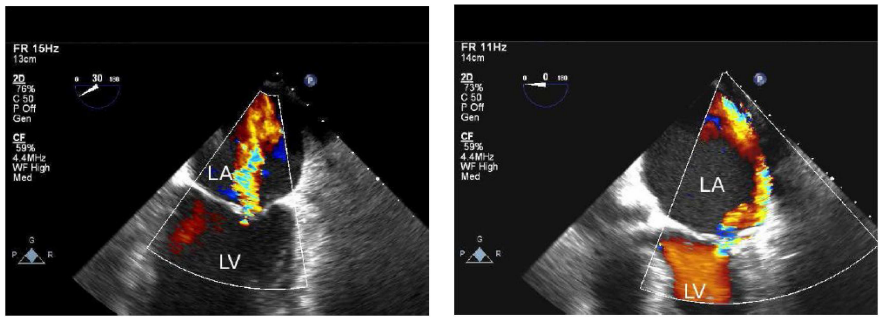

(a) Central color Doppler jet (b) Eccentric color Doppler jet

Figure 2: (a) Echocardiographic image of central regurgitant jet flowing from the left ventricle (LV) to the left atrium (LA). Colors denote different flow velocities. (b) Echocardiographic image of eccentric regurgitant jet, hugging the walls of the left atrium (LA) known as the Coanda effect.

One of the biggest challenges in echocardiographic assessment of mitral regurgitation is Coanda effect: when the regurgitant jet "hugs" the wall of the heart's atrium as shown in Figure 2 (b), the echocardiographic assessment of the severity of MR is contaminated [9, 24]. These eccentric, wall-hugging, non-symmetric regurgitant jets that have been observed at Reynolds numbers well below turbulence [28, 1], appear smaller in the color Doppler image of regurgitant flow (due to the presence of a large secondary vortex), leading to a gross under-estimation of regurgitant volume by inexperienced observers [9, 3]. As a result, patients who may require surgery are left untreated. Understanding the flow conditions and regurgitant orifice geometries responsible for the Coanda effect has been recognized to be of great importance for echocardiographic assessment of mitral valve regurgitation [9].

In our previous works [19, 20, 18], we showed that, once validated, a computational model provides detailed, point-wise information about the quantities that are used in echocardiographic assessment of MR, thereby providing information that can be used to tune and refine the already existing protocols, or design new protocols. Our computational fluid model has been validated against experiments performed in an *in vitro* mock heart chamber shown in Figure 3. The mock heart chamber has been developed by our collaborators at the Methodist DeBakey Heart & Vascular Center [10] to study 2D and 3D color Doppler techniques that are routinely used to image the complex intra-cardiac flows associated with central MR jets [10, 11]. The chamber is composed of two acrylic cylinders partitioned by a divider plate containing a geometric orifice mimicking a leaky mitral valve and it was studied in a variety of clinically relevant flow conditions. However, our collaborators have never been able to reproduce *in vitro* the wall-hugging MR jets typical of the Coanda effect.

Despite of the large cardiovascular and bioengineering literature reporting on the Coanda effect in echocardiographic assessment of mitral regurgitation, there is very little connection with the fluid dynamics literature that could help identify and understand the main features of the corresponding flow conditions. In this paper, our goal is to understand what causes the onset of the Coanda effect in a simplified setting. A mitral regurgitant jet flows from the left ventricle through an orifice between the mitral leaflets, called regurgitant orifice, into the left atrium. As a simplified setting, which has the same geometric features as MR, we consider contraction-expansion channels. First, we focus on the planar case (see Fig. 4(a)) and investigate the influence of the Reynolds number defined in eq. (6) and the expansion ratio $\lambda = W/w$, where W and w are defined in Fig. 4(a). Then, we consider a 2D geometry corresponding to a section of the mock heart chamber (see Fig. 8) in order to understand the role played by certain geometric features on triggering the Coanda effect. Finally, we will

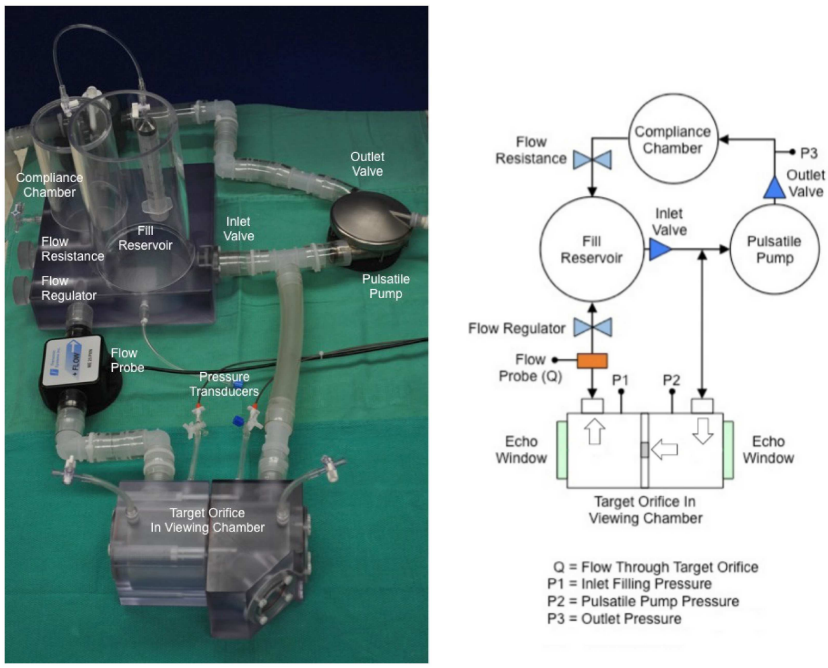

(a) Flow loop photo

(b) Flow loop scheme

Figure 3: Experimental set-up: (a) picture of the flow loop with the mock heart chamber at the bottom of the picture and (b) its schematic representation.

propose a 3D mock heart chamber geometry in which the Coanda effect can be reproduced and explain why it is unlikely to observe such an effect in the chamber currently used to simulate regurgitant flow in mitral valve regurgitation, shown in Fig. 3(a).

The outline of the paper is as follows. In Section 2 we state the problem, discuss the numerical methods used for the time and space discretization and describe the solution of the associated linear system. In Section 3, we report on the results of the validation against [15] and [6]. In Section 4, we discuss the results for the flow in the mock heart chamber. Finally, conclusions are drawn in Section 5.

2 Numerical modeling

The fluid in the mock heart chamber is water with 30% glycerin added to mimic blood viscosity (0.035 poise). The motion of such a fluid, which is incompressible, viscous, and Newtonian, in a spatial domain of dimension d (denoted hereafter by Ω) over a time interval of interest $(0, T)$ is described by the incompressible Navier-Stokes equations:

$$\rho\left(\frac{\partial \boldsymbol{u}}{\partial t} + \boldsymbol{u}\cdot\nabla\boldsymbol{u}\right) - \nabla\cdot\boldsymbol{\sigma} = \mathbf{0} \qquad \text{in } \Omega\times(0,T), \tag{1}$$

$$\nabla\cdot\boldsymbol{u} = 0 \qquad \text{in } \Omega\times(0,T), \tag{2}$$

where ρ is the fluid density, $\boldsymbol{u}$ is the fluid velocity, and $\boldsymbol{\sigma}$ the Cauchy stress tensor. For Newtonian fluids, $\boldsymbol{\sigma}$ has the following expression

$$\boldsymbol{\sigma}(\boldsymbol{u}, p) = -p\mathbf{I} + 2\mu\boldsymbol{\epsilon}(\boldsymbol{u}),$$

where p is the pressure, μ is the fluid dynamic viscosity, and

$$\boldsymbol{\epsilon}(\boldsymbol{u}) = \frac{1}{2}(\nabla \boldsymbol{u} + (\nabla \boldsymbol{u})^T)$$

is the strain rate tensor. In eq. (1)-(2), it is supposed that no body force is applied to the system.

Equations (1)-(2) need to be supplemented with initial and boundary conditions:

$$\boldsymbol{u} = \boldsymbol{u}_D \quad \text{on } \partial\Omega_D \times (0,T), \tag{3}$$

$$\boldsymbol{\sigma n} = \boldsymbol{g} \quad \text{on } \partial\Omega_N \times (0,T), \tag{4}$$

$$\boldsymbol{u} = \boldsymbol{u}_0 \quad \text{in } \Omega \times \{0\}. \tag{5}$$

Here $\overline{\partial\Omega_D} \cup \overline{\partial\Omega_N} = \overline{\partial\Omega}$ and $\partial\Omega_D \cap \partial\Omega_N = \emptyset$. In addition $\boldsymbol{u}_D$, $\boldsymbol{g}$ and $\boldsymbol{u}_0$ are given. For all the test cases under consideration $\boldsymbol{g}$ and $\boldsymbol{u}_0$ are set to zero, while $\boldsymbol{u}_D$ will vary as specified in Sections 3 and 4.

The Reynolds number Re can be used to characterize the flow regime. It is defined as:

$$Re = \frac{\rho L U}{\mu}, \tag{6}$$

where L is a characteristic length and U is a characteristic velocity. The Reynolds number can be thought of as the ratio of inertial forces to viscous forces. For large Reynolds numbers inertial forces are dominant over viscous forces and vice versa.

The flow in the 2D geometry reported in Fig. 4(a) can be seen as the limiting case of a 3D flow in the domain shown in Fig. 4(b) for channel depth H tending to infinity. For the 3D problem, the characteristic length L is given by the hydraulic diameter of the contraction channel, i.e. $L = 2Hw/(H+w)$, thus (6) becomes:

$$Re_{3D} = \frac{\rho U}{\mu}\frac{2Hw}{H+w}. \tag{7}$$

By letting $H \to \infty$ in eq. (7), we define the Reynolds number for the 2D problem

$$Re = 2\frac{\rho U w}{\mu}. \tag{8}$$

We define Re as in (8) with the purpose of comparing our results with [15] in Sec. 3 and for the 2D simulations on a section of the mock heart chamber. As characteristic velocity U in (8), we take the average velocity in the contraction channel. So, if we denote by $U_{\max}$ the maximum velocity in the contraction channel and assume that the contraction channel is long enough to have a fully developed parabolic velocity profile, we have $U = 2U_{\max}/3$.

For the 3D simulations in Sec. 4.2 we will use definition (7). As characteristic velocity U in (7), we take again the average velocity in the contraction channel. If we assume that in the contraction channel we have a fully developed parabolic velocity profile with maximum velocity $U_{\max}$, this means $U = U_{\max}/2$.

For the variational formulation of the fluid problem (1)-(2), we denote by $L^2(\Omega)$ the space of square integrable functions in a spatial domain Ω and with $H^1(\Omega)$ the space of the functions in $L^2(\Omega)$ with first derivatives in $L^2(\Omega)$. We use $(\cdot,\cdot)_\Omega$ and $\langle\cdot,\cdot\rangle_\Omega$ to denote the $L^2(\Omega)$ inner product and a duality pairing in Ω, respectively. Moreover, let us define:

$$[H^1_D(\Omega)]^d = \left\{ \boldsymbol{v} \in [H^1(\Omega)]^d,\ \boldsymbol{v}|_{\partial\Omega_D} = \boldsymbol{u}_D \right\},$$

$$[H^1_{0D}(\Omega)]^d = \left\{ \boldsymbol{v} \in [H^1(\Omega)]^d,\ \boldsymbol{v}|_{\partial\Omega_D} = \boldsymbol{0} \right\},$$

where $\partial\Omega_D$ is the part of the domain boundary on which a Dirichlet condition (3) is imposed.

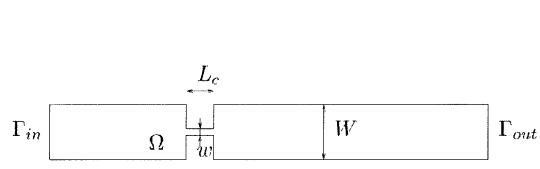

(a) 2D geometry

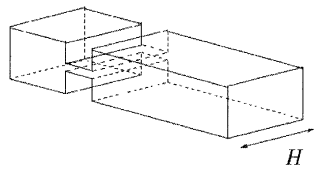

(b) 3D geometry

Figure 4: (a) 2D and (b) 3D contraction-expansion channel. The 2D channel in (a) is the limit case of the 3D channel in (b) for $H \to \infty$.

The variational formulation of the fluid problem (1)-(2) is: given $t \in (0, T)$, find $(\boldsymbol{u}, p) \in [H^1_D(\Omega)]^d \times L^2(\Omega)$ such that

$$\rho\left(\frac{\partial \boldsymbol{u}}{\partial t}, \boldsymbol{v}\right)_\Omega + \mathcal{N}(\boldsymbol{u}; [\boldsymbol{u}, p], [\boldsymbol{v}, q])_\Omega = 0, \quad \forall (\boldsymbol{v}, q) \in [H^1_{0D}(\Omega)]^d \times L^2(\Omega), \tag{9}$$

with

$$\begin{aligned}\mathcal{N}(\boldsymbol{u}; [\boldsymbol{u}, p], [\boldsymbol{v}, q])_\Omega =& 2\mu(\boldsymbol{\epsilon}(\boldsymbol{u}), \boldsymbol{\epsilon}(\boldsymbol{v}))_\Omega + \rho \int_\Omega (\boldsymbol{u} \cdot \nabla \boldsymbol{u}) \cdot \boldsymbol{v} \mathrm{d}\Omega - (p, \nabla \cdot \boldsymbol{v})_\Omega \\ &+ (\nabla \cdot \boldsymbol{u}, q)_\Omega.\end{aligned} \tag{10}$$

The initial condition is given by (5). Notice that for eq. (9) we assumed $\boldsymbol{g} = \boldsymbol{0}$ in (4) as is the case for the numerical tests in Sections 3 and 4.

2.1 Discretization

For the time discretization of equations (1)-(2) we chose the Backward Differentiation Formula of order 2 (BDF2, see [21]). Given $\Delta t \in \mathbb{R}$, let us set $t^n = t_0 + n\Delta t$, with $n = 0, ..., N_T$ and $T = t_0 + N_T \Delta t$. Problem (1)-(2) discretized in time reads: given $\boldsymbol{u}^n$, for $n \geq 0$, find the solution $(\boldsymbol{u}^{n+1}, p^{n+1})$ of the system:

$$\rho \frac{3\boldsymbol{u}^{n+1} - 4\boldsymbol{u}^n + \boldsymbol{u}^{n-1}}{2\Delta t} + \rho \boldsymbol{u}^{n+1} \cdot \nabla \boldsymbol{u}^{n+1} - \nabla \cdot \boldsymbol{\sigma}(\boldsymbol{u}^{n+1}, p^{n+1}) = \boldsymbol{0} \qquad \text{in } \Omega, \tag{11}$$

$$\nabla \cdot \boldsymbol{u}^{n+1} = 0 \qquad \text{in } \Omega. \tag{12}$$

All the numerical test in Sections 3 and 4 are started from fluid at rest, that is we set $\boldsymbol{u}_0 = \boldsymbol{0}$ in (5). Thus, we take $\boldsymbol{u}^{-1} = \boldsymbol{u}^0 = \boldsymbol{0}$.

For the space discretization, we introduce a conformal and quasi-uniform partition $\mathcal{T}_h$ of Ω made up of a certain number of elements (triangles in 2D, tetrahedra in 3D). Let $V_h \subset [H^1(\Omega)]^d$, $V_{D,h} \subset [H^1_D(\Omega)]^d$, $Q_h \subset L^2(\Omega)$ be the finite element spaces approximating $[H^1(\Omega)]^d$, $[H^1_D(\Omega)]^d$, and $L^2(\Omega)$, respectively. We introduce the Lagrange basis $\{\phi_i\}_{i=1}^{\mathcal{N}_v}$ and $\{\pi_i\}_{i=1}^{\mathcal{N}_p}$ associated to V_h and Q_h (respectively), where $\mathcal{N}_v$ is the number of nodes for the velocity approximation and $\mathcal{N}_p$ is number of nodes for the pressure approximation.

In order to write the matrix version of the fully discretized problem, we set:

- The mass matrix: $M_{i,j} = \int_\Omega \rho \phi_j \phi_i$.
- The stiffness matrix: $K_{i,j} = 2\int_\Omega \mu \boldsymbol{\epsilon}(\boldsymbol{\phi}_j) : \boldsymbol{\epsilon}(\boldsymbol{\phi}_i)$.
- The matrix associated with the convective term: $N_{i,j}(\boldsymbol{u}^{n+1}) = \int_\Omega \rho(\boldsymbol{u}^{n+1} \cdot \nabla)\boldsymbol{\phi}_j \cdot \boldsymbol{\phi}_i$.
- The matrix associated with operator $(-\nabla \cdot)$: $B_{i,j} = -\int_\Omega (\nabla \cdot \boldsymbol{\phi}_j)\pi_i$.

The full discretization of problem (1)-(2) yields the following nonlinear system

$$\frac{3}{2\Delta t}M\mathbf{U}^{n+1} + K\mathbf{U}^{n+1} + N(\boldsymbol{u}^{n+1})\mathbf{U}^{n+1} + B^T\mathbf{P}^{n+1} = \mathbf{b}_u^{n+1}, \tag{13}$$

$$B\mathbf{U}^{n+1} = \mathbf{b}_p^{n+1}, \tag{14}$$

where $\mathbf{U}^{n+1}$ and $\mathbf{P}^{n+1}$ are the arrays of nodal values for velocity and pressure. The arrays $\mathbf{b}_u^{n+1}$ and $\mathbf{b}_p^{n+1}$ account for the contributions of the solution at the previous time steps and the contribution that the boundary nodes give to the internal nodes.

Set $C = \frac{3}{2\Delta t}M + K + N(\boldsymbol{u}^{n+1})$. We can rewrite (13)-(14) in the form

$$A\mathbf{X}^{n+1} = \mathbf{b}^{n+1}, \tag{15}$$

where

$$A = \begin{bmatrix} C & B^T \\ B & 0 \end{bmatrix}, \quad \mathbf{X}^{n+1} = \begin{bmatrix} \mathbf{U}^{n+1} \\ \mathbf{P}^{n+1} \end{bmatrix}, \quad \mathbf{b}^{n+1} = \begin{bmatrix} \mathbf{b}_u^{n+1} \\ \mathbf{b}_p^{n+1} \end{bmatrix}.$$

In order to deal with the convective term nonlinearity, we use a fixed-point algorithm. At every fixed-point iteration, we use a multifrontal parallel sparse direct solver (see, e.g., [5]) to solve the linearized version of system (15).

The standard Galerkin approximation of the incompressible Navier-Stokes equations reported in (13)-(14) is unstable if the pair (Q_h, V_h) does not satisfy the well-known *inf-sup* condition (see, e.g. [22]). In order to be able to use equal order velocity-pressure pairs (which are not inf-sup stable, like the $\mathbb{P}_1 - \mathbb{P}_1$ finite elements we used for the results in this paper), we resort to a stabilized formulation.

The stabilization method that we adopt is the orthogonal subgrid scales (OSS) technique proposed in [4]: it provides pressure stability and stabilizes the convective term for high Reynolds numbers. Let $\boldsymbol{u}_h$ and p_h be the space discrete velocity and pressure. The stabilized version of the problem under consideration reads: given $t \in (0,T)$, find $(\boldsymbol{u}_h, p_h) \in V_h \times Q_h$

$$\rho\left(\frac{\partial \boldsymbol{u}_h}{\partial t}, \boldsymbol{v}_h\right)_\Omega + \mathcal{N}_s(\boldsymbol{u}_h; [\boldsymbol{u}_h, p_h], [\boldsymbol{v}_h, q_h])_\Omega = 0, \quad \forall (\boldsymbol{v}_h, q_h) \in V_{D,h} \times Q_h,$$

where $\mathcal{N}(\boldsymbol{u}_h; [\boldsymbol{u}_h, p], [\boldsymbol{v}_h, q_h])_\Omega$ in the discretization of (9) has been replaced by

$$\begin{aligned}\mathcal{N}_s\left(\boldsymbol{u}_h; [\boldsymbol{u}_h, p_h], [\boldsymbol{v}_h, q_h]\right)_\Omega =& \mathcal{N}\left(\boldsymbol{u}_h; [\boldsymbol{u}_h, p_h], [\boldsymbol{v}_h, q_h]\right)_\Omega \\ &+ \mathcal{S}\left(\boldsymbol{u}_h; [\boldsymbol{u}_h, p_h], [\boldsymbol{v}_h, q_h]\right)_\Omega.\end{aligned}$$

The perturbation term $\mathcal{S}$ introduced by OSS (in its quasi-static form) reads

$$\begin{aligned}\mathcal{S}\left(\boldsymbol{u}_h; [\boldsymbol{u}_h, p_h], [\boldsymbol{v}_h, q_h]\right)_\Omega =& (\tau_1 \Pi^\perp(\boldsymbol{u}_h \cdot \nabla \boldsymbol{u}_h + \nabla p_h), \boldsymbol{u}_h \cdot \nabla \boldsymbol{v}_h + \nabla q_h)_\Omega \\ &+ (\tau_2 \Pi^\perp(\nabla \cdot \boldsymbol{u}_h), \nabla \cdot \boldsymbol{v}_h)_\Omega.\end{aligned} \tag{16}$$

Here, $\Pi^\perp(\cdot)$ is the L^2 orthogonal projection onto the finite element space, i.e.: $\Pi^\perp(\cdot) = \mathcal{I}(\cdot) - \Pi(\cdot)$, where $\Pi(\cdot)$ is the L^2 projection onto the finite element space and $\mathcal{I}(\cdot)$ the identity operator. For the choice of the stabilization parameters τ_1 and τ_2 and for a thorough description of this stabilization technique, we refer to [4].

Let us denote by C_s the sum of matrix C and the corresponding stabilization terms obtained from (16). Similarly, we denote by B_s (B_s^T, resp.) the sum of matrix B (B^T, resp.) and the corresponding stabilization terms. Moreover, we denote by L_τ the matrix associated with the pressure stabilization. The stabilized fully discrete problem can be written in matrix form (15) as

$$A = \begin{bmatrix} C_s & B_s^T \\ B_s & L_\tau \end{bmatrix}, \quad \mathbf{X}^{n+1} = \begin{bmatrix} \mathbf{U}^{n+1} \\ \mathbf{P}^{n+1} \end{bmatrix}, \quad \mathbf{b}^{n+1} = \begin{bmatrix} \mathbf{b}_u^{n+1} \\ \mathbf{b}_p^{n+1} \end{bmatrix}.$$

For more details concerning the discretization of the Navier-Stokes problem, we refer to, e.g., [22].

3 Preliminary study of a contraction-expansion channel

The main aim of this section is to validate our solver against the results reported in [15] and [6]. We perform a series of simulations in planar contraction-expansion channels with two different values of the expansion ratio λ to identify the critical Reynolds number Re_{sb} at which the jet ceases to be symmetric (i.e., central; see Fig. 2(a)) to become wall-hugging (i.e., eccentric; see Fig. 2(b)). This is known in the literature as symmetry breaking bifurcation. Once our solver has been validated and convergence studies have been performed showing good convergence properties, it can be used as a predictive tool for discovery of new physical phenomena.

Let us start with the test case in [15]. The geometry under consideration is shown in Fig. 4(a) with the upstream and downstream channel width $W = 4$, and contraction width $w = 0.26$. Thus, the expansion ratio $\lambda = W/w$ is 15.4. The length of the contraction L_c is set to 2. In this domain, we simulate the flow for different Reynolds numbers (ranging from 0.01 to 71.3) to examine the onset of asymmetries.

Eq. (1)-(2) are supplemented with the following steady boundary conditions: parabolic velocity profile at the inlet Γ_{in}, stress-free boundary condition at the outlet Γ_{out}, and no-slip condition on the rest of the boundary. Both the channel upstream of the contraction and the expansion channel need to be long enough so that the flow is fully established when it reaches the contraction and the outlet section. The fluid is initially at rest. A time marching algorithm is used to approach the steady-state solution. The numerical simulations were stopped when the relative L^2-norm of the difference of two subsequent solutions was less that a prescribed tolerance ϵ:

$$\frac{||\mathbf{u}_h^{n+1} - \mathbf{u}_h^n||_{L^2(\Omega)}}{||\mathbf{u}_h^{n+1}||_{L^2(\Omega)}} \leq \epsilon \quad \text{and} \quad \frac{||p_h^{n+1} - p_h^n||_{L^2(\Omega)}}{||p_h^{n+1}||_{L^2(\Omega)}} \leq \epsilon, \tag{17}$$

where $\mathbf{u}_h^{n+1}$ (resp., $\mathbf{u}_h^n$) and p_h^{n+1} (resp., p_h^n) are the computed velocity and pressure at time t^{n+1} (resp., t^n). The value of ϵ was set to 10^{-8}.

In Fig. 5, we report the streamlines at the time when stopping criterion (17) is satisfied for four different values of Re. For very low Reynolds number (e.g., $Re = 0.01$), it is impossible to deduce the flow direction from the streamlines: as shown in Fig. 5(a), the flow has both a horizontal and vertical symmetry axis. As the Reynolds number is increased, the Moffatt eddies (see [14]) downstream of the expansion grow while the vortices upstream of the contraction reduce in size: we see in Fig. 5(b) that the flow at $Re = 7.8$ has lost the symmetry about the vertical axis, while the symmetry about the horizontal axis is maintained. At a further increase of the Reynolds number, the flow becomes asymmetric also with respect to the horizontal symmetry axis of the domain; see Fig. 5(c) which corresponds to $Re = 31.1$. In Fig. 5(c), the lower recirculation enlarged and pushed the high velocity jet to the upper wall. Notice that the flow could have evolved to its reflected image configuration with respect to the domain symmetry axis. A further increase in Reynolds number generates a third vortex downstream on the side of the smaller primary vortex, as the enlarged one grows and pushes the jet even closer to the wall; see Fig. 5(d). Fig. 5 is in good qualitative agreement with [15].

It was shown [26, 8, 25, 13] that this behavior occurs as a result of a supercritical pitchfork bifurcation in the solution of the Navier Stokes equations, i.e., above Re_{sb} two stable solutions co-exist [2]. Bifurcation theory allows to clarify the nature of the multiplicity of possible flows, whereas a (numerical or laboratory) experiment will give one or the other of the stable asymmetric solutions. The asymmetric solution remains stable for a certain range of Re and asymmetries become stronger with the increasing Reynolds number, as shown in [12]. The formation of stable asymmetric vortices in 2D planar expansion is due to the Coanda effect (see [29]): an increase in velocity near one wall will lead to a decrease in pressure near that wall and once a pressure difference is established across the channel it will maintain the

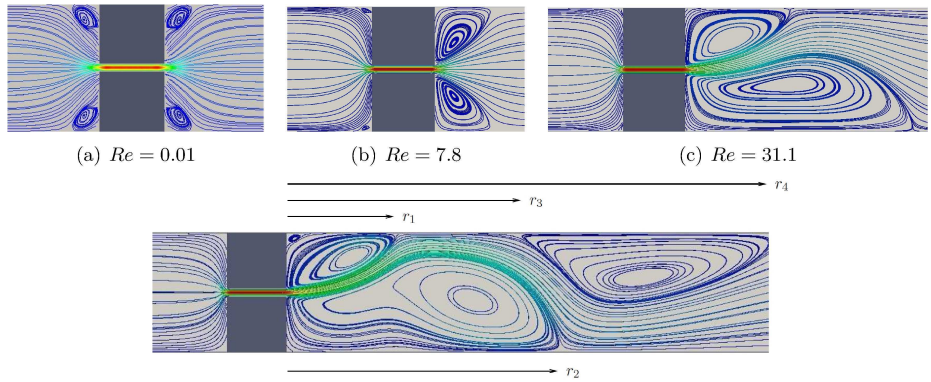

(a) $Re = 0.01$ (b) $Re = 7.8$ (c) $Re = 31.1$

(d) $Re = 71.3$

Figure 5: Expansion ratio $\lambda = 15.4$: Streamlines at the time when stopping criterion (17) is satisfied for Reynolds numbers (a) $Re = 0.01$, (b) $Re = 7.8$, (c) $Re = 31.1$, (d) $Re = 71.3$. The streamlines are colored with the velocity magnitude, with blue corresponding to 0 and red corresponding to 1.

asymmetry of the flow. The value of Re_{sb} has been identified for different expansion ratios λ. In particular, it was found that Re_{sb} decreases with increasing value of λ (see [6, 23, 13]).

For a quantitative agreement, we report the bifurcation diagram shown in Fig. 6, which shows the effect of the Reynolds number on the length of the recirculation zones formed downstream of the expansion and it is identical to the one presented in [15]. The lengths in Fig. 6 (r_1 to r_4, as marked in Fig. 5(d)) are normalized with respect to the downstream channel width W. As in [15], the critical Reynolds number for the symmetry breaking Re_{sb} was found to be approximately 28.5, which is in good agreement also with the results in [12]. In fact, reference [12] considers $\lambda = 16$ and obtains a critical Reynolds number of 27.5, which is very close to what we get. At Re between 41 and 42, the third vortex appears.

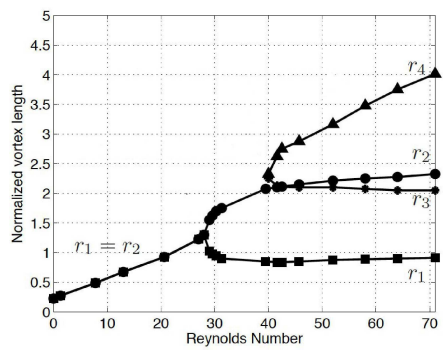

Figure 6: Expansion ratio $\lambda = 15.4$: bifurcation diagram for the geometry shown in Fig. 4(a).

For a further validation of the results, we consider a test case from [6]. Since we are only interested in the evolution of the vortices in the expansion channel as Re varies, we are going to consider the domain reported in Fig. 7(a): the inlet Γ_{in} of this new geometry is the outlet of the contraction channel in Fig. 4(a). The expansion chamber width W is set to 1 and

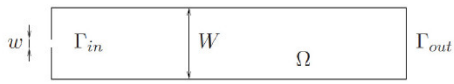

(a) Geometry considered in [6]

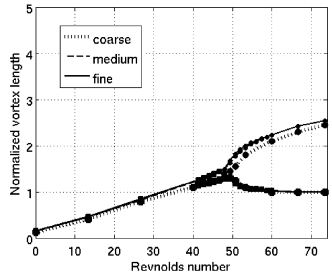

(b) Bifurcation diagram for $\lambda = 6$

Figure 7: (a) Computational geometry considered in [6] and (b) a convergence study for the bifurcation diagram corresponding to the 2D flow in such geometry with $\lambda = 6$. The results refer to three different meshes: coarse, medium, and fine.

the contraction width w is equal to $1/6$, which implies $\lambda = 6$. This is one of the geometries considered in [6]. Note that if the contraction channel length L_c (see Fig. 4) is large enough to have an established Poiseuille flow in it, the flow upstream of the contraction is not going to affect the flow downstream. In this domain, we examine the onset of asymmetries by simulating the flow for Reynolds numbers ranging from 0.01 to 73.3.

As boundary conditions, we impose a parabolic velocity profile with maximum velocity $U_{\max} = 1$ on Γ_{in}, a stress-free boundary condition at the outlet Γ_{out}, and no-slip condition on the rest of the boundary. We change the Reynolds number by varying the value of the viscosity μ. The stopping tolerance for the fixed point iterations was set to 10^{-8}, since as the Reynolds number increases the convective term needs to be properly resolved.

For this second test case, we checked the influence of the mesh size on the value of Re_{sb}. Three meshes with different levels of refinement were considered:

- a coarse mesh, with an average element diameter $h_{avg} = 4 \cdot 10^{-2}$, a maximum element diameter $h_{max} = 6 \cdot 10^{-2}$ and a minimum element diameter $h_{min} = 10^{-2}$; this mesh has around 10^4 nodes and $1.9 \cdot 10^4$ triangles;

- a medium mesh, with $h_{avg} = 2.3 \cdot 10^{-2}$, $h_{max} = 4 \cdot 10^{-2}$, $h_{min} = 7 \cdot 10^{-3}$; this mesh has around $2.2 \cdot 10^4$ nodes and $4.3 \cdot 10^4$ triangles;

- a fine mesh, with $h_{avg} = 1.3 \cdot 10^{-2}$, $h_{max} = 2.8 \cdot 10^{-2}$, $h_{min} = 5 \cdot 10^{-3}$; this mesh has around $4.4 \cdot 10^4$ nodes and $8.7 \cdot 10^4$ triangles.

The minimum diameter was set at the inlet in order to have proper resolution of the contraction. The bifurcation diagram in Fig. 7(b) shows the effect of Reynolds number on the length of the recirculation regions. Since now $W = 1$, the normalized lengths correspond to the actual lengths.

From Fig. 7(b) we see that for $\lambda = 6$ the third recirculation does not appear for $Re \leq 73.3$, regardless of the mesh used, while for $\lambda = 15.4$ it appeared just past $Re = 41$. We observe that the results for the medium mesh and the fine mesh are almost superimposed and they both give a value of Re_{sb} approximately equal to 46.5. Notice that as the aspect ratio λ decreases, the critical Reynolds number for the symmetry breaking increases, as observed also in [6]. The bifurcation graph in Fig. 7(b) is very similar to the one in [6], taking into account the fact that we defined the Reynolds number as in (8) with the characteristic velocity $U = 2U_{\max}/3$, while in [6] the Reynolds number is defined as in (6) with $L = w$ and $U = U_{\max}$, $U_{\max}$ being the maximum inlet velocity. Converting our value $Re_{sb} = 46.5$ to the system used in [6] we get 34.8, which is very close to 33, the value found in [6]. Fig. 7(b)

shows that if the computations are performed on a mesh that is under-refined, the value of Re_{sb} gets overestimated.

At larger Reynolds number the flow becomes increasingly complex and other bifurcations occur. At a further increase of Re, the flow becomes unsteady and the existence of a Hopf bifurcation is deduced [26]. In [17], for $\lambda = 6$ we showed that a Hopf bifurcation does occur in the expansion channel: at a certain Reynolds number the asymmetric solution loses its stability and a one-parameter family of periodic solutions bifurcates from the stationary solution.

4 Numerical results for the mock heart chamber

In this section, we first consider the flow in a section of the mock heart chamber. This 2D study sheds some light on the causes of the Coanda effect and helps us understand how to construct a 3D mock heart chamber in which the Coanda effect can be reproduced. Finally, we comment on why it is unlikely to observe such an effect in the current mock heart chamber shown in Fig. 3(a).

4.1 A section of the chamber

Let us consider the radial section of the real chamber parallel to the horizontal chamber walls in Fig. 3(a). The geometry of this section is a contraction-expansion channel with expansion ratio $\lambda = 45$. Notice that the inlet and outlet sections for this channel differ from those in Fig. 4(a). In fact, the fluid enters end exits the mock heart chamber through two tubes whose dimeter is smaller that the chamber diameter. We changed inlet and outlet with respect to the channels in the previous section to reflect the flow configuration in the real chamber.

Based on the results reported in Sec. 3, we expect the wall-hugging effect to appear at a very low Reynolds number since the channel under consideration has $\lambda = 45$. In Fig. 8, we report the streamlines at the time when stopping criterion (17) is satisfied for three different values of Re. For a Reynolds number equal to 2, the jet expands in the center of the expansion chamber as shown in Fig. 8(a). Notice that due to the modified inlet and outlet sections, we cannot refer to the jet in Fig. 8(a) as symmetric, however there is clearly no wall-hugging effect taking place. As the Reynolds number is increased to 20, the upper downstream recirculation zone becomes bigger than the lower recirculation: the jet is pulled towards the outlet, yet again no Coanda effect is displayed; see Fig. 8(b). At $Re = 100$ instead, the jet hugs the lower wall before reaching the outlet as shown in Fig. 8(c). Moreover, from $Re = 20$ to $Re = 100$ secondary recirculations have appeared and the flow has become increasingly complex.

In Sec. 3, we noted that if the contraction channel length L_c (see Fig. 4(a)) is large enough to have established Poiseuille flow in it, the flow upstream of the contraction is not going to affect the flow downstream. In the geometry under consideration the contraction channel length is very small because "healthy" mitral valve leaflets have a thickness of less than 5 mm. For this reason, we decided to check whether different flows upstream of the contraction lead to different flows in the expansion chamber. We report in Fig. 9 the streamlines at the time when the stopping criterion (17) is satisfied for $Re = 100$ and two inlet configurations: inlet at the left vertical wall (as for the channels in Sec. 3) and inlet as in the real chamber (i.e., as in Fig. 8). Fig. 9 shows that also for a short contraction channel length the flow upstream of the contraction does not influence the flow in the expansion chamber.

If the Reynolds number is further increased from 100 the solution becomes time-dependent, indicating that a Hopf bifurcation has occurred. Thus, increasing the Reynolds number is not a viable way to make the Coanda effect more pronounced. In the following, we are going to consider a couple of geometry modifications that will push the jet to the wall almost throughout its entire length, as observed *in vivo* (see Fig. 2 (b)).

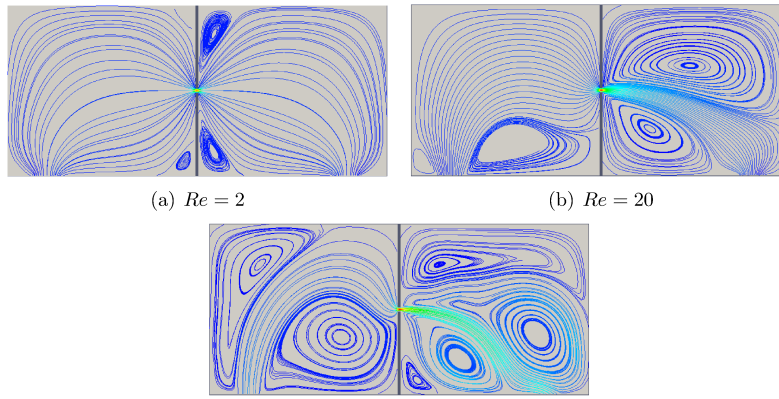

(a) $Re = 2$ (b) $Re = 20$

(c) $Re = 100$

Figure 8: Streamlines in a section of the mock heart chamber for different values of Reynolds number: (a) $Re = 2$, (b) $Re = 20$, and (c) $Re = 100$.

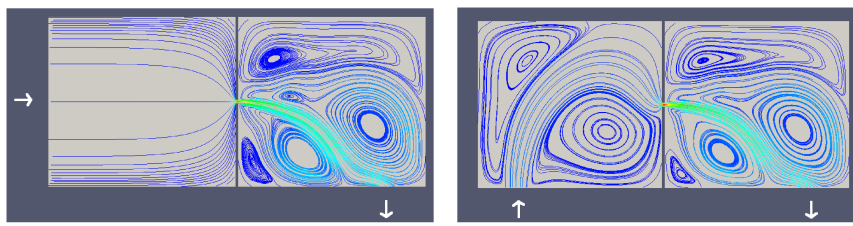

(a) Large vertical inlet (b) Small horizontal inlet

Figure 9: Streamlines for $Re = 100$ in a section of the mock heart chamber for two inlet configurations: (a) inlet at the left vertical wall and (b) inlet as in the real chamber. The arrows indicate the flow direction.

The mitral valve is a bi-leaflet valve. The anterior leaflet covers approximately two-thirds of the total valve surface. See Fig. 10(a). This means that the orifice between the leaflets is unlikely to form in the center of the valve. For this reason, we consider an orifice closer to the lower wall (see Fig. 11(a)) rather than in the center (see Fig. 8). Moreover, mitral valve prolapse, which is characterized by the displacement of a mitral valve leaflet into the left atrium as shown in Fig. 10(b), is typically observed in patients with eccentric regurgitant jets. Therefore we consider the geometry with an uneven orifice reported in Fig. 11(b).

Fig. 11(a) shows that when the orifice is closer to the lower wall the recirculation below the jet in the expansion chamber is smaller than in the case of a central orifice, so the wall-hugging effect becomes more pronounced. Compare Fig. 11(a) with Fig. 9(a), which were both obtained for $Re = 100$. In the case of an uneven orifice (i.e., prolapsed valve), the jet hugs the lower wall along its entire length. See Fig. 11(b), which also corresponds to $Re = 100$.

In summary, this 2D study in a section of the real chamber indicates that an evident Coanda effect can be achieved thanks to two geometry modifications: lowering the location of the orifice (closer to the outlet), and making the orifice plate uneven. Next, we are going to use these conclusions to construct a 3D mock heart chamber in which the Coanda effect can be reproduced.

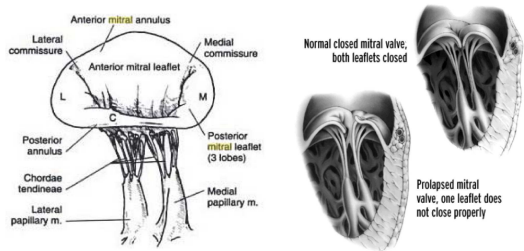

(a) Mitral valve anatomy (b) Mitral valve prolapse

Figure 10: (a) Anatomy of the mitral valve [16] and (b) comparison between a normal mitral valve and a prolapsed mitral valve.

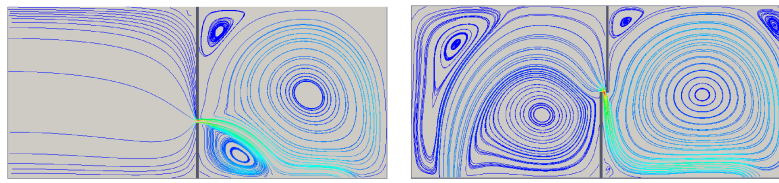

(a) Lower orifice (b) Uneven orifice

Figure 11: Streamlines for $Re = 100$ in a section of the mock heart chamber for two modified orifice configurations: (a) lower orifice and (b) uneven orifice.

4.2 A 3D chamber with quasi-2D flow

In [15], the 3D channel in Fig. 4(b) was considered and an extensive set of simulations was carried out for expansion ratio $\lambda = 14.5$ and variable aspect ratio $\chi = H/w$. The goal was to understand how the flow varies in a 3D contraction-expansion channel as the Reynolds number (defined in eq. (7)) and χ change.

Let us introduce dimensionless variable $\mathcal{H} = H/(H + w) = \chi/(\chi + 1)$: the values of $\mathcal{H}$ is bounded between 0, for $\chi = 0$ which corresponds to the Hele-Shaw flow limit, and 1, for $\chi \to \infty$ which corresponds to the 2D flow limit. It was found in [15] that for low $\mathcal{H}$ and low Re_{3D}, there is no visible recirculation formed downstream of the expansion. For $Re_{3D} > 28.5$, which corresponds to the critical value for the symmetry breaking in 2D for $\lambda = 14.5$, the sequence of events when $\mathcal{H}$ varies is as follows. For low $\mathcal{H}$ (e.g., 0.01) the flow still resembles an irrotational flow. As $\mathcal{H}$ increases, small vortices form at the outlet of the contraction channels. These vortices, called "lip vortices", form only in the three-dimensional flow and they are not observed in the planar case. When $\mathcal{H}$ reaches the value of 0.5, in addition to the lip vortices, corner vortices appear. The latter are the Moffatt eddies observed also in the bi-dimensional flow (see Fig. 5(a)). A further increase of $\mathcal{H}$ leads to the formation of full corner recirculations as those in Fig. 5(b). Only for high values of $\mathcal{H}$ (e.g., 0.8), asymmetric flow with large recirculations is observed.

The results in [15] show that the vertical walls in Fig. 4(b) have a stabilizing effect on the flow patterns by inhibiting the onset of flow asymmetries, i.e. fully three-dimensional flow prevents the flow asymmetries observed in quasi-2D flow at the same Reynolds number. In fact, the results in [15] indicate that the asymmetric solution, corresponding to the Coanda effect, is obtained for larger Reynolds numbers and for channels with larger normalized depth $\mathcal{H}$. Since $\mathcal{H} = H/(H + w)$, where w is the width of the contraction channel and H is the depth, this implies that Coanda effect occurs for the contraction channels which are

slender ($w << H$). This information can be related to the studies of Coanda effect in mitral regurgitation: the depth of the channel corresponds to the regurgitant orifice length, while the width of the channel corresponds to the orifice width. Therefore, the Coanda effect is expected to occur for regurgitant orifices which are long and narrow, i.e., for those for which $w << H$.

The mitral valve leaflets, when the valve is closed, make contact along a relatively long region, called coaptation. See Figure 12(a). In regurgitant valves when the two leaflets do not close properly, the length of the coaptation region that stays open corresponds to the depth in the contraction channel, denoted by H in Figure 12. Thus, in the case of mitral valve regurgitation, one can expect to see Coanda effect in cases when the regurgitation occurs along a large portion of the mitral coaptation and at larger Reynolds numbers.

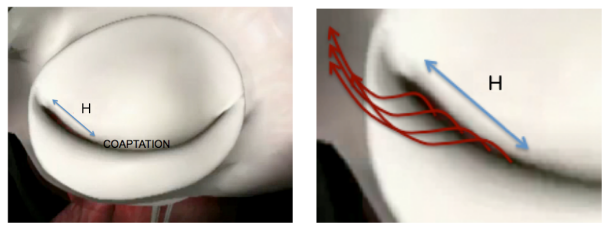

(a) (b)

Figure 12: (a) Sketch of a closed regurgitant mitral valve, viewed from the top (left atrium) and (b) sketch of an eccentric regurgitant jet in the magnified view of the valve in (a).

We test our hypotheses by constructing a 3D mock heart chamber with a slender orifice: we extrude the section of the real chamber considered in Sec. 4.1 to achieve aspect ratio $\chi = 45$, corresponding to $\mathcal{H} = 0.98$. See Fig. 13. Notice in Fig. 13(b) that the extrusion generates also elongated inlet and outlet sections.

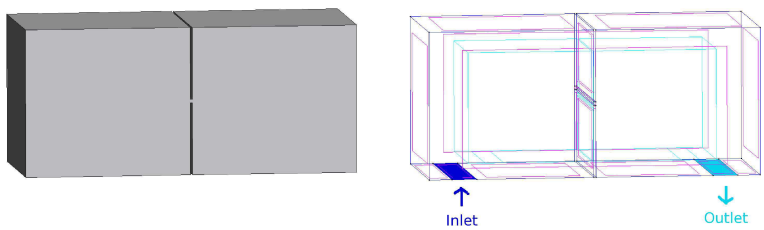

(a) 3D chamber for quasi-2D flow (b) Chamber skeleton

Figure 13: (a) 3D chamber generated by extruding the section of the real chamber considered in Sec. 4.1. (b) Skeleton of the chamber in (a).

We report in Fig. 14 the streamlines at the time when stopping criterion (17) is satisfied for $Re_{3D} = 100$ and two orifice configurations: even and uneven orifice. In the case of the even orifice shown in Fig. 14(a), the big recirculation below the jet in the expansion chamber prevents an evident wall-hugging effect, as already observed in 2D (see Fig. 8(c)). On the other hand, the jet passed through the uneven orifice hugs the expansion chamber walls along its entire length, as shown in Fig. 14(b).

Fig. 15 shows the velocity magnitude on the central vertical section of the geometry in Fig. 13(a) for both the even and the uneven orifice. Notice how closely the flow resembles the corresponding 2D flow in Fig. 8(c) and 11(b), respectively. This shows that far away from the vertical wall the flow does not feel the presence of the walls. This 3D chamber succeeds

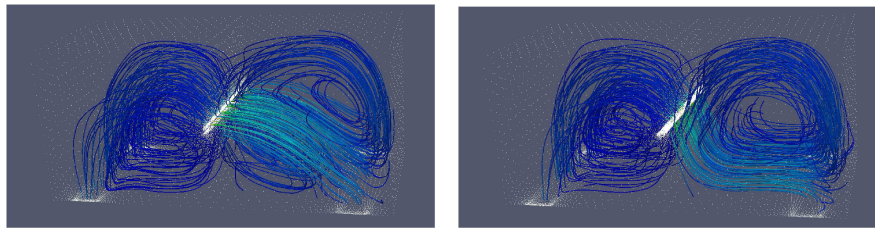

(a) Even orifice (b) Uneven orifice

Figure 14: Streamlines in the 3D chamber shown in Fig. 13(a) for Reynolds number $Re_{3D} = 100$ and two orifice configurations: (a) even orifice and (b) uneven orifice.

in producing quasi-2D flow, thereby allowing the Coanda effect at the low Reynolds numbers for which it is observed in 2D.

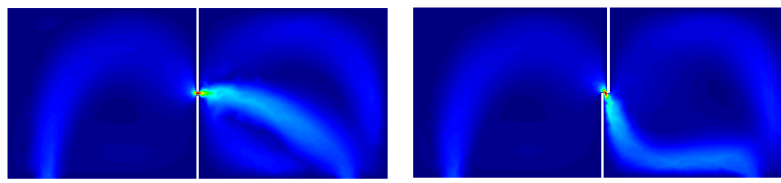

(a) Even orifice (b) Uneven orifice

Figure 15: Velocity magnitude on the central vertical section of the geometry in Fig. 13(a) for two orifice configurations: (a) even orifice and (b) uneven orifice.

For the uneven orifice, which corresponds to a prolapsed valve, we compared our numerical results with experimental data acquired by Magnetic Resonance Imaging in Fig. 16. The qualitative comparison is excellent.

The 3D chamber proposed in this section successfully recreates the Coanda effect because it allows for quasi-2D flow since it is made of two cubes, it has elongated (rectangular) inflow and outflow sections, and a slender orifice. The real chamber shown in Fig. 3(a) is made of two cylinders, it has small (circular) inflow and outflow sections and a small orifice. Thus, the flow in the real chamber is fully 3D, inhibiting the onset of wall-hugging jets. For this reason, it is unlikely to observe such an effect in the real mock heart chamber.

5 Conclusions

We presented a numerical study aimed at understanding the causes of the Coanda effect in 2D and 3D contraction-expansion channels. The dynamics of these systems were analyzed by means of direct numerical simulation of the unsteady NavierStokes equations. This was a first step towards establishing a connection between the large cardiovascular and bioengineering literature reporting on the Coanda effect in echocardiographic assessment of mitral regurgitation and the fluid dynamics literature. The long term goal of this work is to improve the diagnosis of mitral valve regurgitation for eccentric, wall-hugging jets.

In contraction-expansion channels, a steady symmetric flow is observed for sufficiently small values of the Reynolds number. Above a certain critical Reynolds number, a steady asymmetric solution is observed: recirculation zones of different sizes form on the upper and lower wall. We validated the critical Reynolds number for the symmetry-breaking bifurcation given by our computations against the value in [15] for expansion $\lambda = 15.4$ and the value in

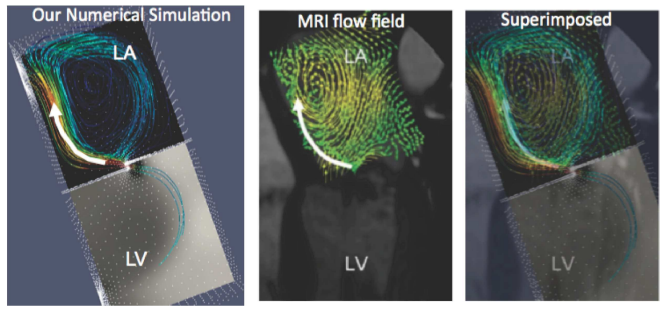

Figure 16: Qualitative comparison between our simulation of flow in the mock left atrium (LA) chamber and Magnetic Resonance Imaging of flow in LA [7]. The fluid is flowing from the left ventricle (LV). Flow streamlines are shown.

[6] for $\lambda = 6$. Excellent agreement was found.

Next, we considered the flow in a section of the mock heart chamber our medical collaborators use to reproduce in vitro the cardiac hemodynamics encountered in patients with MR. Such a section is a 2D contraction-expansion channel with a large expansion ratio ($\lambda = 45$). Through a series of numerical simulations we show that a pronounced Coanda effect is possible only with some modifications of the orifice (i.e., contraction channel) geometry. Thanks to these results and the results in 3D contraction-expansion channels reported in [15], we argue that in the real chamber the fully three-dimensional flow prevents the wall-hugging effect observed in 2D flow at the same Reynolds number.

Finally, we propose a 3D mock heart chamber in which quasi-2D flow is possible, thereby allowing the Coanda effect at the low Reynolds numbers for which it is observed in 2D.

Acknowledgements

This research has been supported in part by the National Science Foundation under grants DMS-1318763, DMS-1311709, and DMS-0806941 (Canic), DMS-1263572 and DMS-1109189 (Canic and Quaini), and by the Texas Higher Education Board (ARP-Mathematics) 003652-0023-2009 (Canic and Glowinski).

Dr. S. Little from the Methodist Hospital in Houston is gratefully acknowledged for the medical images and the pictures of the experimental set-up. The authors would also like to thank Professor Hishida from University of Nagoya for giving them the opportunity to contribute to the proceedings of a most exciting Navier-Stokes equations dedicated workshop.

References

[1] J. Albers, T. Nitsche, J. Boese, R. De Simone, I. Wolf, A. Schroeder, and . F. Vahl. Regurgitant jet evaluation using three-dimensional echocardiography and magnetic resonance. *Ann Thorac Surg*, 78:96–102, 2004.

[2] F. Battaglia, S.J. Tavener, A.K. Kulkarni, and C.L. Merkle. Bifurcation of low Reynolds number flows in symmetric channels. *AIAA J.*, 35:99–105, 1997.

[3] K. Chao, V.A. Moises, R. Shandas, T. Elkadi, D.J. Sahn, and R. Weintraub. Influence of the Coanda effect on color Doppler jet area and color encoding. *Circulation*, 85:333–341, 1992.

[4] R. Codina. Stabilized finite element approximation of transient incompressible flows using orthogonal subscales. *Comput. Methods Appl. Mech. Engrg.*, 191:4295–4321, 2002.

[5] T.A. David and I.S. Duff. An unsymmetric-pattern multifrontal method for sparse LU factorization. *SIAM. J. Matrix Anal. & Appl.*, 18(1):140–158, 1997.

[6] D. Drikakis. Bifurcation phenomena in incompressible sudden expansion flows. *Phys. Fluids*, 84:76–87, 1978.

[7] P. Dyverfeldt, J. Kvitting, C. C. ll, G. Boano, A. Sigfridsson, U. Hermansson, A. F. Bolger, J. Engvall, and T. Ebbers. Hemodynamic aspects of mitral regurgitation assessed by generalized phase-contrast MRI. *Journal of Magnetic Resonance Imaging*, page 33:582588, 2011.

[8] R.M. Fearn, T. Mullin, and K.A. Cliffe. Nonlinear flow phenomena in a symmetric sudden expansion. *J. Fluid Mech.*, 211:595–608, 1990.

[9] C. Ginghina. The Coanda effect in cardiology. *J. Cardiovasc. Med.*, 8:411–413, 2007.

[10] S. H. Little, S.R. Igo, M. McCulloch, C. J. Hartley, Y. Nosé, and W. A. Zoghbi. Three-dimensional ultrasound imaging model of mitral valve regurgitation: design and evaluation. *Ultrasound in Med. & Biol.*, 34(4):647–654, 2008.

[11] S. H. Little, S.R. Igo, B. Pirat, M. McCulloch, C. J. Hartley, Y. Nosé, and W. A. Zoghbi. In vitro validation of real-time three-dimensional color Doppler echocardiography for direct measurment of Proximal Isovelocity Surface Area in mitral rigurgitation. *Am. J. Cardiol.*, 99(10):1440–1447, 2007.

[12] S. Mishra and K. Jayaraman. Asymmetric flows in planar symmetric channels with large expansion ratios. *Int. J. Num. Meth. Fluids*, 38:945–962, 2002.

[13] J. Mizushima, H. Okamoto, and H. Yamaguchi. Stability of flow in a channel with a suddenly expanded part. *Physics of Fluids*, 8(11):2933–2942, 1996.

[14] H.K. Moffatt. Viscous and resistive eddies near a sharp corner. *J. Fluid Mech.*, 18:1–18, 1964.

[15] M.S.N. Oliveira, L.E. Rodd, G.H. McKinley, and M.A. Alves. Simulations of extensional flow in microrheometric devices. *Microfluid Nanofluid*, 5:809–826, 2008.

[16] C. M. Otto. *Valvular Heart Disease. Edition 2.* Elsevier. The Curtis Center. Philadelphia, 2002.

[17] A. Quaini, S. Canic, and R. Glowinski. Symmetry breaking and preliminary results about a Hopf bifurcation for incompressible viscous flow in an expansion channel. *Int. J. Comput. Fluid Dyn.*, published online, 2016.

[18] A. Quaini, S. Canic, R. Glowinski, S.R. Igo, C.J. Hartley, W.A. Zoghbi, and S.H. Little. Validation of a 3D computational fluid-structure interaction model simulating flow through an elastic aperture. *J. Biomech.*, 45(2):310–318, 2012.

[19] A. Quaini, S. Canic, G. Guidoboni, R. Glowinski, S. Igo, C. Hartley, W. Zoghbi, and S. Little. Numerical simulation of an ultrasound imaging model of mitral valve regurgitation. Abstract in Valves in the Heart of the Big Apple VI: Evaluation and Management of Valvular Heart Diseases 2010. *Cardiology*, 115:251–293, 2010.

[20] A. Quaini, S. Canic, G. Guidoboni, R. Glowinski, S.R. Igo, C.J. Hartley, W.A. Zoghbi, and S.H. Little. A three-dimensional computational fluid dynamics model of regurgitant mitral valve flow: validation against *in vitro* standards and 3D color Doppler methods. *Cardiovascular Engineering and Technology*, 2(2):77–89, 2011.

[21] A. Quarteroni, R. Sacco, and F. Saleri. *Numerical Mathematics.* Springer Verlag, 2007.

[22] A. Quarteroni and A. Valli. *Numerical Approximation of Partial Differential Equations.* Springer-Verlag, 1994.

[23] A. Revuelta. On the two-dimensional flow in a sudden expansion with large expansion ratios. *Phys. Fluids*, 17(1):1–4, 2005.

[24] A. Schmidt, O.C. Almeida, A. Pazin, J.A. Marin-Neto, and B.C. Maciel. Valvular regurgitation by color Doppler echocardiography. *Arq. Bras. Cardiol.*, 74(3):273–281, 2000.

[25] M. Shapira, D. Degani, and D. Weihs. Stability and existence of multiple solutions for viscous flow in suddenly enlarged channels. *Comp. Fluids*, 18:239–258, 1990.

[26] I.J. Sobey and P.G. Drazin. Bifurcations of two-dimensional channel flows. *J. Fluid Mech.*, 171:263–287, 1986.

[27] D.J. Tritton. *Physical Fluid Dynamics (Section 22.7, The Coanda Effect).* (reprinted 1980). Van Nostrand Reinhold, 1977, 1980.

[28] M. Vermeulen, R. Kaminsky, B. Van Der Smissen, T. Claessens, P. Segers, P. Verdonck, and Peter Van Ransbeeck. In vitro flow modelling for mitral valve leakage quantification. *Proc. 8th Int. Symp. Particle Image Velocimetry*, August 25-28, 2009.

[29] R. Wille and H. Fernholz. Report on the first European mechanics colloquium on Coanda effect. *J. Fluid Mech.*, 23:801–819, 1965.